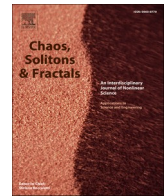




ELSEVIER

Contents lists available at [ScienceDirect](https://www.sciencedirect.com)

# Chaos, Solitons and Fractals

journal homepage: [www.elsevier.com/locate/chaos](http://www.elsevier.com/locate/chaos)

## A quadratic BSDE framework for risk-adjusted noise-induced switching in bistable nonlinear oscillators under stochastic volatility

Dong Feng<sup>a</sup><sup>a</sup> Faculty of Civil Engineering, RWTH Aachen University, Mies-van-der-Rohe-Strafte 1, 52074, Aachen, Germany

## ARTICLE INFO

## Keywords:

Quadratic BSDE  
Stochastic volatility  
Bistable switching  
Intermittency  
Entropic risk  
Rare event

## ABSTRACT

Noise-induced transitions between coexisting attractors are ubiquitous in nonlinear devices and natural systems, yet risk quantification becomes nontrivial when excitation intensity is intermittent and exhibits volatility clustering. We propose a quadratic backward stochastic differential equation (BSDE) approach to compute a dynamic, risk-adjusted switching metric for bistable oscillators driven by stochastic volatility. The forward dynamics couples a double-well drift with a Cox–Ingersoll–Ross-type variance process and correlated Brownian motions, capturing bursts of agitation often observed in ambient vibrations and complex environments. For an overload or switching payoff at a terminal horizon, we adopt the entropic risk measure, leading to a quadratic BSDE whose exponential transform is a martingale. This yields a numerically stable regression Monte Carlo algorithm that estimates the time-resolved conditional risk along trajectories and constructs parametric risk surfaces with respect to initial state and volatility. Numerical experiments demonstrate that volatility and cross-correlation strongly modulate the probability–risk gap: regimes with comparable raw switching probabilities may exhibit markedly different risk profiles under risk aversion. The proposed BSDE-based metric provides an early-warning indicator for impending transitions and a practical tool for robust design and reliability assessment of bistable nonlinear systems under intermittent stochastic forcing.

### 1. Introduction

Noise-driven transitions between coexisting attractors are a defining mechanism of complex behavior in nonlinear dynamical systems [1–4]. In bistable settings, the deterministic drift organizes phase space into basins of attraction separated by an unstable saddle, while stochastic excitation provides the fluctuations required for barrier crossing [5–7]. This interplay underpins response regimes in bistable mechanical elements, snap-through structures, and reduced-order models of tipping phenomena [8–11]. Beyond its engineering relevance, bistable switching is also a canonical scenario for studying rare events, metastability, and non-equilibrium transport in nonlinear stochastic systems [12–14]. In addition, related bistable stochastic models have been used in quantitative finance to represent market instabilities and regime shifts [15,16]. In that setting, nonlinear drift terms, including cubic potentials, are combined with stochastic volatility to capture volatility clustering [17–19]. This connection provides additional context for the present modeling choices and motivates transferring risk-sensitive tools to intermittently forced nonlinear systems.

Most analytical and computational studies of bistable switching assume stationary excitation with constant intensity [20–22].

*E-mail address:* [dong.feng@rwth-aachen.de](mailto:dong.feng@rwth-aachen.de).

<https://doi.org/10.1016/j.chaos.2026.118021>

Received 29 December 2025; Received in revised form 26 January 2026; Accepted 2 February 2026

Available online 5 February 2026

0960-0779/© 2026 The Author.

Published by Elsevier Ltd.

This is an open access article under the CC BY license

(<http://creativecommons.org/licenses/by/4.0/>).

Under this assumption, long-time statistics can be related to stationary Fokker–Planck descriptions, and switching rates can often be approximated through asymptotic arguments in the weak-noise limit [23,24]. In many practical environments, however, the forcing intensity varies over time and exhibits intermittency, meaning that quiescent periods are punctuated by bursts of elevated agitation [25–28]. Such volatility clustering is widely documented in measured vibration environments and in complex stochastic media, and it leads to strongly non-Gaussian response statistics [29–31]. In this regime, mean switching probabilities and mean overload levels may remain moderate, while extreme episodes dominate the operational risk [32–34].

This motivates reliability metrics that are sensitive to tail behavior and that remain consistent when updated in time as new information becomes available. Dynamic risk measures provide such a framework by assigning, at each time, a conditional assessment of future losses based on the current filtration. Among them, the entropic risk criterion is particularly suitable for stochastic dynamics because it yields a time-consistent nonlinear conditional expectation with a clear large-deviation interpretation [35–37]. Importantly, the entropic criterion admits a backward stochastic differential equation (BSDE) representation with a quadratic driver, thereby linking tail-aware risk quantification to the established theory of quadratic BSDEs and, through Markov representations, to semilinear parabolic partial differential equations (PDEs) with quadratic gradient terms [38–40].

The present work develops a quadratic BSDE approach to risk-adjusted switching and overload quantification in bistable nonlinear systems driven by stochastic-volatility excitation. The forward model couples a double-well drift to a nonnegative mean-reverting variance process with correlated noise channels, allowing systematic investigation of intermittency strength and state–intensity coupling. The backward component evaluates the dynamic entropic risk of a terminal switching or overload functional, and an exponential transform converts the quadratic BSDE into a martingale suitable for stable regression Monte Carlo estimation. This combination yields time-resolved conditional risk trajectories and parametric risk surfaces, enabling a direct comparison between probability-based switching descriptors and tail-sensitive, risk-adjusted indicators under intermittent stochastic forcing.

## 2. Forward model: bistable oscillator under stochastic volatility

Consider a filtered probability space  $(\Omega, \mathcal{F}, \{\mathcal{F}_t\}_{t \in [0, T]}, \mathbb{P})$  supporting a two-dimensional Brownian motion  $W_t = (W_t^{(1)}, W_t^{(2)})$ . The bistable state  $X_t$  follows the overdamped stochastic dynamics:

$$\begin{aligned} dX_t &= b(X_t)dt + \sqrt{V_t}dW_t^{(1)} \\ b(x) &= x - x^3 \end{aligned} \tag{1}$$

with initial condition  $X_0 = x_0$ . The drift  $b(x)$  corresponds to a symmetric double-well potential  $U(x) = \frac{1}{4}x^4 - \frac{1}{2}x^2$ , since  $b(x) = -U'(x)$ . The equilibria near  $x = \pm 1$  are stable and the point  $x = 0$  is unstable, providing the classical bistable geometry underlying switching.

To represent intermittent excitation intensity, the instantaneous variance  $V_t$  is modeled as a nonnegative mean-reverting diffusion of Cox–Ingersoll–Ross (CIR) type [41,42]:

$$dV_t = \kappa(\theta - V_t)dt + \sigma_v \sqrt{V_t}dW_t^{(2)} \tag{2}$$

where  $\kappa > 0$  is the reversion rate,  $\theta > 0$  the long-run mean level, and  $\sigma_v > 0$  the volatility. This choice is appropriate when the forcing amplitude is empirically observed to fluctuate over time with bursts and clustering, while remaining strictly nonnegative.

The two Brownian components are correlated according to:

$$\begin{aligned} d\langle W^{(1)}, W^{(2)} \rangle_t &= \rho dt \\ \rho &\in [-1, 1] \end{aligned} \tag{3}$$

This correlation plays a mechanistic role by coupling episodes of elevated variance to the state fluctuations that facilitate barrier crossing. This introduces an additional dimension of dynamical complexity beyond constant-intensity additive noise.

The pair  $(X_t, V_t)$  forms a Markov diffusion in  $\mathbb{R} \times \mathbb{R}_+$  [43]. For sufficiently smooth  $\varphi(x, v)$ , the generator  $\mathcal{L}$  is given by:

$$\mathcal{L}\varphi = b(x)\partial_x\varphi + \kappa(\theta - v)\partial_v\varphi + \frac{1}{2}v\partial_{xx}\varphi + \rho\sigma_v v\partial_{xv}\varphi + \frac{1}{2}\sigma_v^2 v\partial_{vv}\varphi \tag{4}$$

which will be used to establish the semilinear PDE representation associated with the backward component.

## 3. Target functional and quadratic BSDE based on entropic risk

Let  $T > 0$  be a fixed terminal horizon and define a terminal loss  $\xi$  as a function of the state at time  $T$ . Two common choices that encode barrier-related risk are an overload loss and a switching indicator. The overload loss is defined by:

$$\begin{aligned} \xi &= g(X_T) \\ g(x) &= (x - x_{thr})^+ \end{aligned} \tag{5}$$

where  $x_{thr}$  may be chosen as the saddle location 0 or as a more conservative safety threshold. This payoff is Lipschitz and typically yields better numerical stability. The switching indicator may be defined as:

$$\xi = \mathbf{1}_{\{X_T > 0\}} \tag{6}$$

which directly targets basin change but introduces discontinuity and may require smoothing or increased sampling for regression accuracy.

Risk is quantified through the dynamic entropic risk functional with risk aversion parameter  $\gamma > 0$ :

$$Y_t = \rho_t(\xi) = \frac{1}{\gamma} \ln \mathbb{E}[\exp(\gamma \xi) | \mathcal{F}_t] \tag{7}$$

$$t \in [0, T]$$

As  $\gamma \rightarrow 0$ , the functional converges to the conditional expectation  $\mathbb{E}[\xi | \mathcal{F}_t]$ . For larger  $\gamma$ , the criterion increasingly emphasizes tail contributions, thereby distinguishing regimes with similar mean losses but different extremes. From a practical standpoint,  $\gamma$  reflects the degree of conservatism in penalizing rare but severe switching events relative to typical behavior. In engineering applications,  $\gamma$  can be calibrated to represent a desired safety margin or reliability requirement by choosing  $\gamma$  such that the resulting entropic risk matches an accepted design criterion, such as a prescribed value at risk or conditional value at risk level, an empirically acceptable loss threshold inferred from historical or experimental data, or a cost model that assigns larger penalties to extreme events. In practice,  $\gamma$  may also be treated as a tunable parameter and selected through sensitivity analysis over a plausible range consistent with allowable failure probability and the relative penalty assigned to tail events.

The process  $Y_t$  admits a BSDE representation. There exists a predictable process  $Z_t \in \mathbb{R}^2$  such that:

$$Y_t = \xi + \int_t^T \frac{\gamma}{2} \|Z_s\|^2 ds - \int_t^T Z_s^T dW_s \tag{8}$$

or, in differential form:

$$dY_t = -\frac{\gamma}{2} \|Z_t\|^2 dt + Z_t^T dW_t \tag{9}$$

The driver  $f(z) = \frac{\gamma}{2} \|z\|^2$  exhibits quadratic growth, and direct discretization of  $Y$  may become unstable when  $\gamma$  is moderate or when  $V_t$  produces occasional large fluctuations.

A stabilizing step is obtained through an exponential transform. Let us define:

$$U_t = \exp(\gamma Y_t) \tag{10}$$

By Itô's formula and the structure of the driver [44],  $U_t$  is a positive martingale:

$$U_t = \mathbb{E}[\exp(\gamma \xi) | \mathcal{F}_t] \tag{11}$$

$$dU_t = \Lambda_t^T dW_t$$

$$\Lambda_t = \gamma U_t Z_t$$

This representation converts the quadratic BSDE into the estimation of conditional expectations of  $\exp(\gamma \xi)$  and of its martingale increments, a task well-suited to regression Monte Carlo [45].

When  $(X_t, V_t)$  is a Markov process, one may write  $Y_t = u(t, X_t, V_t)$ . Under standard regularity conditions,  $u$  satisfies the semilinear PDE:

$$\partial_t u + \mathcal{L}u + \frac{\gamma}{2} \|\Sigma^T \nabla u\|^2 = 0 \tag{12}$$

$$u(T, x, v) = g(x)$$

where  $\Sigma$  is the diffusion matrix of  $(X, V)$ . The quadratic gradient term aligns with the quadratic BSDE driver and provides an additional theoretical interpretation of the risk criterion as a nonlinear deformation of the classical backward Kolmogorov equation [46].

#### 4. Numerical method: regression Monte Carlo based on the transformed martingale

Let  $t_n = n\Delta t$  for  $n = 0, \dots, N$  with  $\Delta t = \frac{T}{N}$ , and simulate  $M$  independent paths of the forward model. Correlated Gaussian increments may be generated by:

$$\Delta W_n^{(1)} = \sqrt{\Delta t} Z_n^{(1)} \tag{13}$$

$$\Delta W_n^{(2)} = \sqrt{\Delta t} \left( \rho Z_n^{(1)} + \sqrt{1 - \rho^2} Z_n^{(2)} \right)$$

where  $Z_n^{(1)}$  and  $Z_n^{(2)}$  are independent standard normal variates.

A practical positivity-preserving discretization for the CIR variance uses full truncation:

$$V_{n+1} = \max\left(0, V_n + \kappa(\theta - \max(V_n, 0))\Delta t + \sigma_v \sqrt{\max(V_n, 0)} \Delta W_n^{(2)}\right) \tag{14}$$

The state update is then:

$$X_{n+1} = X_n + (X_n - X_n^3)\Delta t + \sqrt{\max(V_n, 0)}\Delta W_n^{(1)} \tag{15}$$

The backward component is computed through the martingale  $U_t = \exp(\gamma Y_t)$ . At terminal time:

$$U_N^{(m)} = \exp\left(\gamma g\left(X_N^{(m)}\right)\right) \tag{16}$$

$m = 1, \dots, M$

For earlier times, the martingale property implies:

$$U_n = \mathbb{E}[U_{n+1}|X_n, V_n] \tag{17}$$

which is approximated through regression. Let  $\{\phi_k(x, v)\}_{k=1}^K$  denote a set of basis functions and write:

$$U_n \approx \sum_{k=1}^K \beta_{n,k} \phi_k(X_n, V_n) \tag{18}$$

Coefficients are obtained by least squares over simulated samples:

$$\beta_n = \underset{\beta \in \mathbb{R}^K}{\operatorname{argmin}} \sum_{m=1}^M \left( U_{n+1}^{(m)} - \sum_{k=1}^K \beta_k \phi_k(X_n^{(m)}, V_n^{(m)}) \right)^2 \tag{19}$$

To maintain numerical stability when computing  $Y_n = \gamma^{-1} \log U_n$ , the regressed values may be clipped below by a small  $\varepsilon > 0$ :

$$U_n^{(m)} \leftarrow \max\{U_n^{(m)}, \varepsilon\} \tag{20}$$

When the BSDE control  $Z_n$  is required, it can be recovered from the discrete martingale increment representation. Since the following holds:

$$U_{n+1} - U_n \approx \Lambda_n^T \Delta W_n \tag{21}$$

Then we have:

$$\Lambda_n \approx \frac{1}{\Delta t} \mathbb{E}[U_{n+1} \Delta W_n | X_n, V_n] \tag{22}$$

Once again employing component-wise regression, the objective is  $U_{n+1} \Delta W_n^{(i)}$ . The control is then obtained from:

$$Z_n = \frac{\Lambda_n}{\gamma U_n} \tag{23}$$

Although many applications only require  $Y_0$  or  $u(0, x_0, v_0)$ , estimating  $Z$  supports internal consistency checks and can be used to develop variance reduction or risk-sensitive control extensions.

Numerical credibility is strengthened by reporting diagnostics. The following identity holds:

$$U_0 = \mathbb{E}[\exp(\gamma \xi)] \tag{24}$$

This permits a direct Monte Carlo estimate from terminal samples that should be consistent with the regression-based  $U_0$ . Sensitivity to basis choice, time discretization, and sample size should also be examined to ensure that the reported risk measures are not artifacts of regression instability.

### 5. Numerical experiments

This section should demonstrate how stochastic volatility and correlation modify switching risk beyond what is captured by

**Table 1**  
Benchmark values.

Symbol	Meaning	Value
$T$	Terminal horizon	10
$N$	Number of time steps	100
$\Delta t$	Time step size	0.1
$M$	Number of Monte Carlo paths	500
$d$	Polynomial basis degree in regression	2
$\kappa$	Mean-reversion rate	2
$\theta$	Long-run mean	0.15
$x_{thr}$	Overload threshold	0
$\sigma_v$	Volatility-of-volatility	Baseline: 0.6; Parameter scanning: {0, 0.2, 0.4, 0.6, 0.8, 1.0}
$\rho$	Correlation between $W^{(1)}$ and $W^{(2)}$	Baseline: 0.3; Parameter scanning: {-0.8, -0.4, -0.1, 0.1, 0.4, 0.8}
$\gamma$	Risk-aversion parameter	Baseline: 5; Parameter scanning: {1, 2, 4, 6, 8, 10}

probability alone. A suitable baseline uses  $T$  on the order of ten nondimensional units with a time step that resolves the drift and diffusion scales, and a Monte Carlo ensemble large enough to stabilize regression in the presence of intermittent bursts. Then, the benchmark values employed in this numerical study are presented in Table 1, after which  $\sigma_v$ ,  $\rho$ , and  $\gamma$  are used for parameter scans.

The primary outputs are the risk-neutral expectation  $\mathbb{E}[\xi]$  and the risk-adjusted quantity:

$$Y_0 = \frac{1}{\gamma} \log \mathbb{E}[\exp(\gamma \xi)] \tag{25}$$

When  $\xi$  is an overload loss,  $\mathbb{E}[\xi]$  provides a mean overload benchmark. When  $\xi$  is an indicator,  $\mathbb{E}[\xi]$  equals the switching probability  $\mathbb{P}(X_T > 0)$ . In both cases, comparing  $\mathbb{E}[\xi]$  to  $Y_0$  reveals how tail exposure changes under intermittency and risk aversion.

Fig. 1 illustrates the coupled forward dynamics and the associated dynamic risk quantity. The upper panel shows sample paths of the bistable state  $X(t)$ . Most trajectories remain near the left potential well around  $X \approx -1$ , while a small subset exhibits large excursions and approaches or crosses the barrier region, reflecting the typical sparsity of noise-induced switching in multistable systems. The middle panel reports the stochastic volatility  $V(t)$ , which stays nonnegative and displays intermittent bursts. Because the diffusion intensity of the state scales as  $\sqrt{V(t)}$ , these bursts correspond to short intervals of amplified stochastic forcing. The timing of the largest excursions in  $X(t)$  is consistent with such high-volatility episodes, supporting the interpretation that intermittency in excitation intensity promotes barrier approach and switching. The lower panel presents the dynamic entropic risk  $Y(t)$  (see Eq. (7)) reconstructed from the regression estimate of  $U(t)$  (see Eq. (10)). The near-zero values for most times indicate low conditional risk away from the terminal horizon. The appearance of very large negative values close to  $T$  is not expected for a nonnegative terminal loss and suggests a numerical artifact from regression underestimation of  $U(t)$  in the final steps. In practice, this can be mitigated by enforcing a structure-preserving lower bound for  $U(t)$  when  $\xi \geq 0$ , and by improving regression stability through larger sample size, mild regularization, or enriched basis functions near the barrier region.

Fig. 2 examines trajectory-level coupling between the bistable state, the stochastic volatility, and the dynamic entropic risk. For each selected realization, the left panel overlays the state  $X(t)$  and the volatility  $V(t)$ , while the right panel shows the corresponding conditional risk process  $Y(t)$ . This layout highlights how short-lived increases in excitation intensity and barrier proximity jointly influence the risk signal. Across the displayed trajectories,  $Y(t)$  evolves smoothly over most of the horizon and tends to increase when the system exhibits either sustained drift toward the barrier region or pronounced volatility activity. In trajectories where  $X(t)$  departs from the left-well neighborhood and approaches less stable regions, the associated  $Y(t)$  typically rises, reflecting an increase in the conditional expectation of the terminal loss under the entropic transform. Episodes of elevated  $V(t)$  provide an additional mechanism for risk escalation, as higher  $V(t)$  amplifies the instantaneous diffusion of  $X(t)$  and thereby raises the likelihood of large terminal deviations. The late-time behavior is also informative. Several realizations show an upturn of  $Y(t)$  close to  $T$ , which is consistent with the fact that the remaining time to recover decreases and the conditional distribution of the terminal payoff becomes more sensitive to the current state and volatility. Overall, the figure supports interpreting  $Y(t)$  as an early-warning indicator in a probabilistic sense: it increases prior to, and in anticipation of, trajectories that are more likely to end with larger terminal overload or switching-related loss under intermittent excitation.

Fig. 3 quantifies how the parameter  $\sigma_v$  alters both risk-neutral switching statistics and the risk-sensitive assessment provided by the entropic criterion. The three panels are complementary: the top panel reports the initial entropic risk  $Y_0$  for multiple risk-aversion levels  $\gamma$ , the middle panel reports risk-neutral benchmarks, and the bottom panel reports the probability–risk gap. In the top panel,  $Y_0$  increases overall as  $\sigma_v$  grows, and the separation between curves becomes more pronounced for larger  $\gamma$ . This behavior is consistent with the role of  $\sigma_v$  in generating clustered high-volatility episodes in  $V(t)$ . Larger  $\sigma_v$  increases the likelihood and magnitude of transient amplification of the diffusion intensity of  $X(t)$ , which in turn enhances the contribution of rare but severe terminal outcomes. The

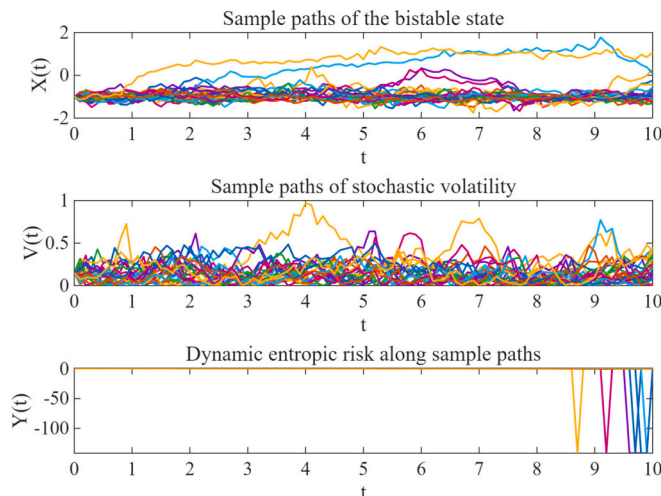


Fig. 1. Ensemble sample paths of the bistable state, stochastic volatility, and dynamic entropic risk.

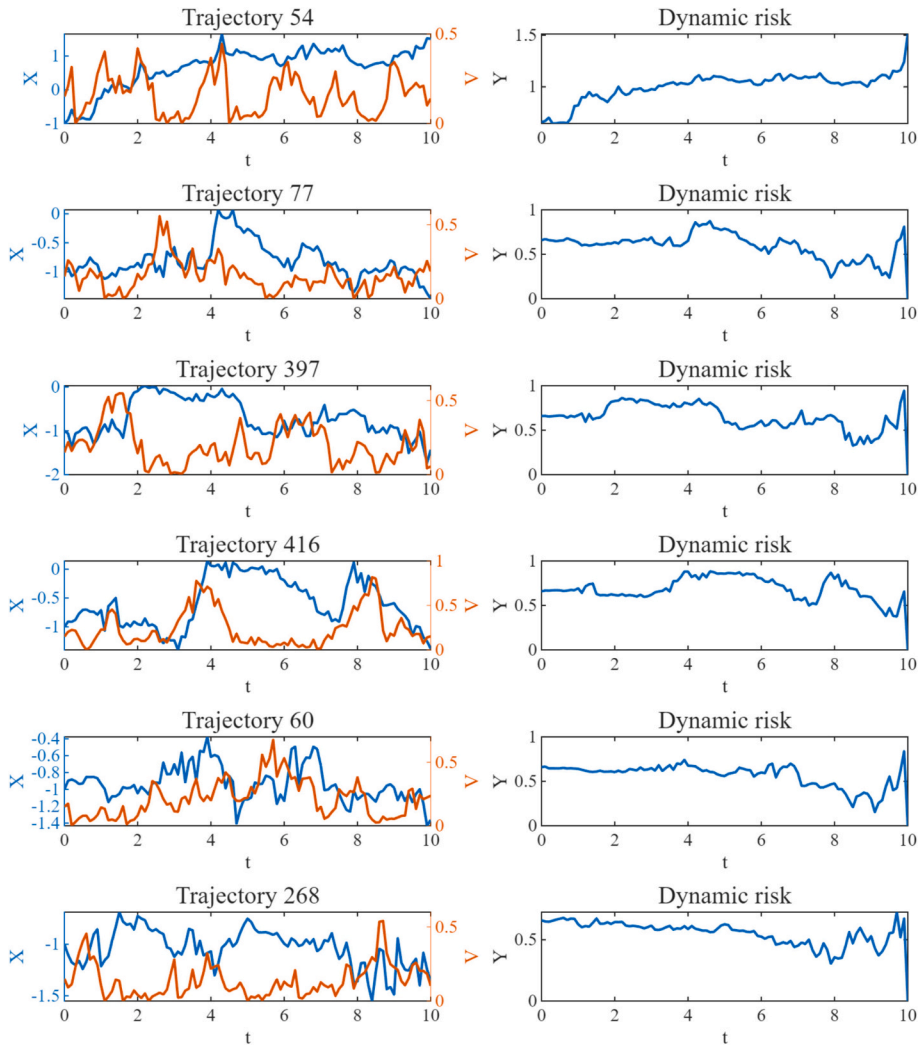


Fig. 2. Early-warning behavior of the dynamic entropic risk along representative trajectories.

stronger growth of  $Y_0$  at higher  $\gamma$  reflects the exponential weighting of tail events inherent to the entropic risk. The middle panel shows that the risk-neutral benchmarks, namely the mean terminal loss  $\mathbb{E}[\xi]$  and the switching probability  $\mathbb{P}(X_T > 0)$ , also increase with  $\sigma_v$ , but on a comparatively smaller scale. This indicates that intermittency modifies the overall propensity for barrier crossing, yet the effect on average metrics remains moderate relative to the effect on risk-sensitive measures. The bottom panel makes this contrast explicit. The probability–risk gap grows with both  $\sigma_v$  and  $\gamma$ , demonstrating that regimes with similar risk-neutral behavior can exhibit substantially different risk profiles once tail sensitivity is introduced. In practical terms, increasing  $\sigma_v$  does not merely shift the mean response; it reshapes the distribution by strengthening the influence of burst-driven excursions, and this redistribution is captured more sharply by  $Y_0$  than by probability-based summaries.

Fig. 4 characterizes how the correlation parameter  $\rho$  between the state noise and the volatility noise modifies both the risk-neutral switching statistics and the entropic risk assessment. The top panel reports the initial entropic risk  $Y_0$  for multiple levels of risk aversion  $\gamma$ . The middle panel presents risk-neutral benchmarks, including the mean terminal loss  $\mathbb{E}[\xi]$  and the switching probability  $\mathbb{P}(X_T > 0)$ . The bottom panel reports the probability–risk gap, highlighting discrepancies between risk-sensitive and risk-neutral summaries. The top panel shows that  $Y_0$  increases as  $\rho$  moves from negative to positive values, with the sensitivity being more pronounced for larger  $\gamma$ . This indicates that positive correlation strengthens the contribution of adverse trajectories under the entropic transform. Mechanistically, when  $\rho > 0$ , upward fluctuations in the volatility driver tend to align with state-noise increments, increasing the likelihood that high-volatility episodes coincide with state excursions toward and across the barrier. Conversely, negative correlation tends to reduce this alignment, thereby lowering risk at the same volatility level. The middle panel exhibits a similar monotonic dependence in the risk-neutral benchmarks, with both  $\mathbb{E}[\xi]$  and  $\mathbb{P}(X_T > 0)$  increasing with  $\rho$ . The magnitude of change is moderate compared to the top panel, which suggests that correlation influences not only average switching propensity but also the tail structure of terminal outcomes, to which entropic risk is more sensitive. The bottom panel makes this contrast explicit. The probability–risk gap expands with increasing

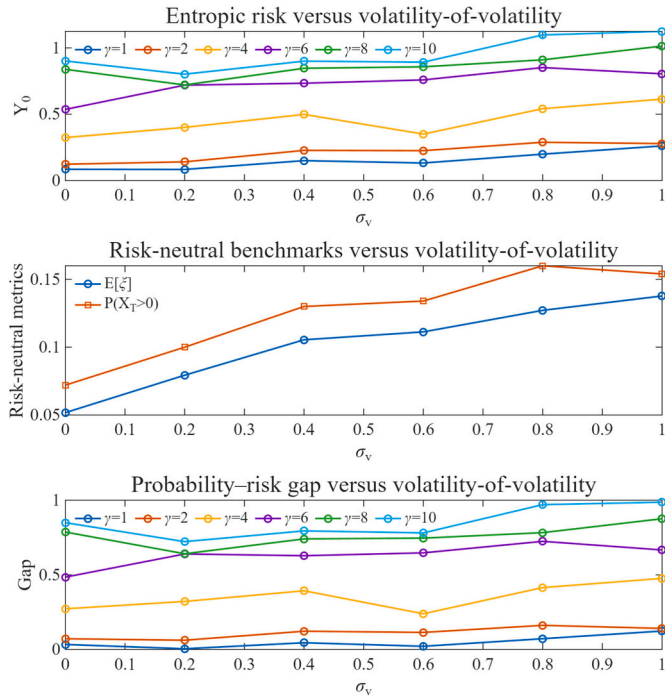


Fig. 3. Sensitivity to  $\sigma_v$ : entropic risk, risk-neutral metrics, and probability-risk gap.

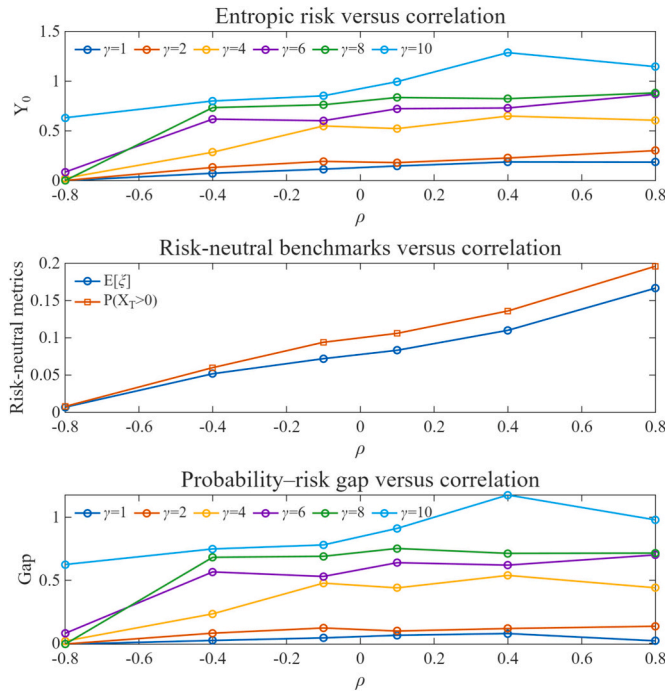
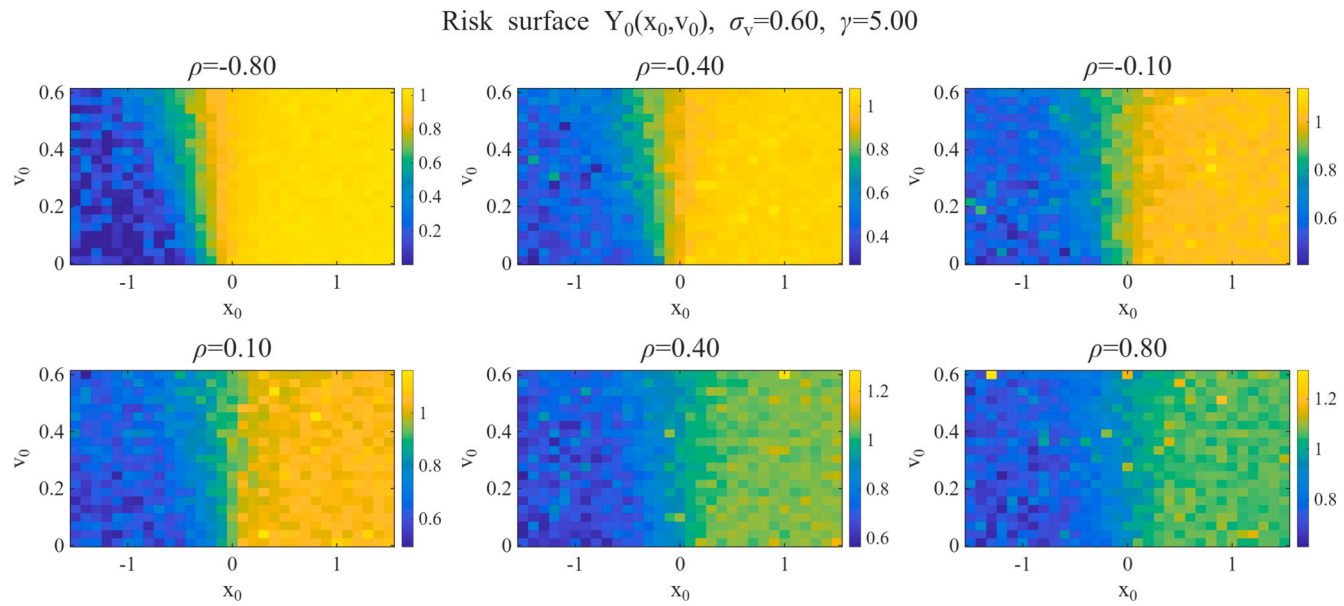


Fig. 4. Sensitivity to  $\rho$ : entropic risk, risk-neutral metrics, and probability-risk gap.

$\rho$  and with increasing  $\gamma$ . This behavior supports the interpretation that correlation acts as a coupling mechanism that reshapes rare-event pathways: positive  $\rho$  concentrates probability mass into more extreme realizations during volatility bursts, while negative  $\rho$  disperses trajectories and reduces the effective severity of burst-driven excursions. Overall, the figure demonstrates that correlation is a structurally important parameter for risk-aware switching assessment, and its influence cannot be captured reliably using probability-



**Fig. 5.** Risk landscape in the state–volatility plane: heat maps of  $Y_0(x_0, y_0)$  across correlations.

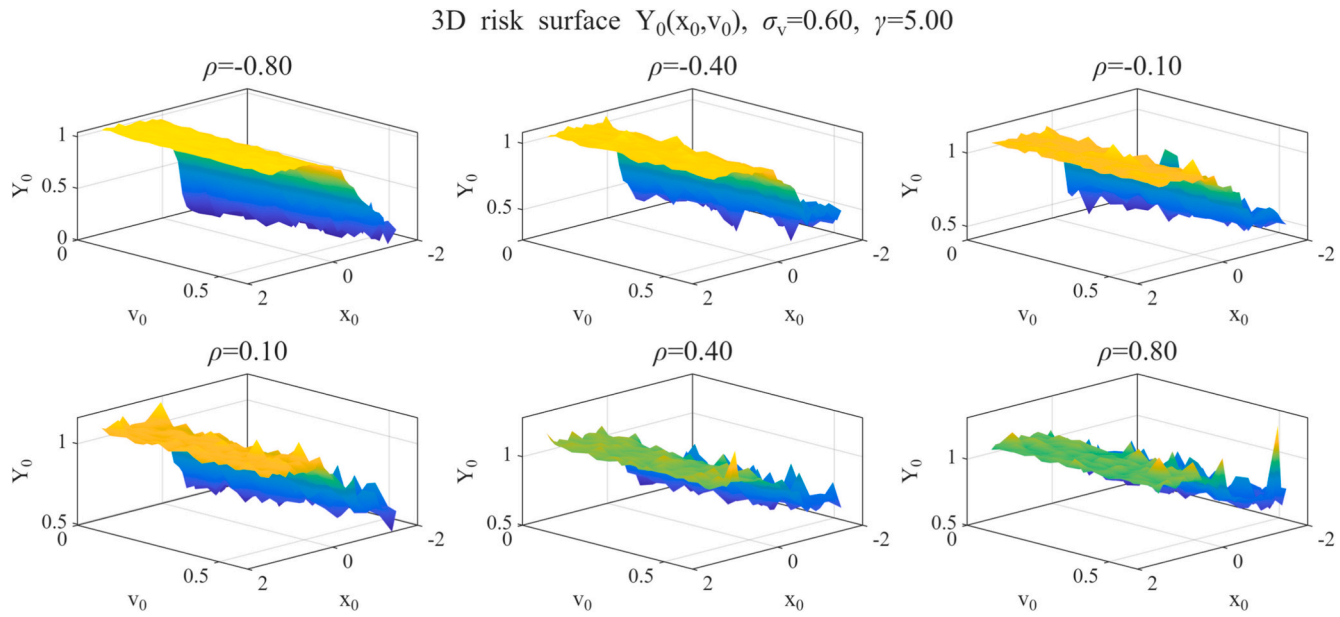


Fig. 6. Risk landscape in the state–volatility plane: three-dimensional surfaces of  $Y_0(x_0, y_0)$  across correlations.

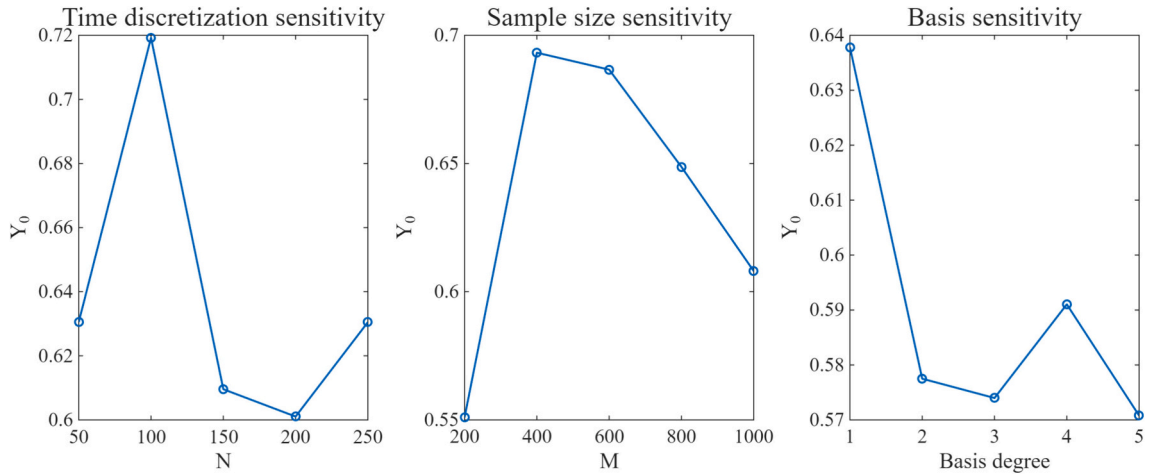


Fig. 7. Numerical robustness of the regression Monte Carlo BSDE solver: sensitivity to time step, sample size, and basis order.

based metrics alone.

Fig. 5 visualizes the initial entropic risk  $Y_0$  as a function of the initial condition  $(x_0, v_0)$  for a fixed volatility and risk aversion, while varying the correlation parameter  $\rho$ . Each panel is a heat map over the state–volatility plane, and together the panels provide a geometric representation of how correlation reshapes the risk landscape. Across all correlation values, a dominant feature is the strong dependence on the initial state  $x_0$ . Lower risk values concentrate in the negative  $x_0$  region, corresponding to initial conditions deep inside the left potential well. As  $x_0$  approaches and crosses the barrier region near  $x_0 \approx 0$ , the risk increases sharply, consistent with the increased likelihood of terminal overload or basin change when the system starts closer to the separatrix. The transition in color across  $x_0$  therefore reflects the basin structure of the underlying bistable drift. The dependence on the initial volatility level  $v_0$  is present but weaker than the dependence on  $x_0$ . For fixed  $x_0$ , larger  $v_0$  generally elevates  $Y_0$ , indicating that higher initial excitation intensity increases the conditional contribution of adverse terminal outcomes under the entropic transform. This effect is most visible near the barrier region, where small increases in diffusion intensity more efficiently translate into barrier approach and excursions. The correlation parameter  $\rho$  modifies the shape and steepness of the risk transition across the separatrix. Moving from negative to positive  $\rho$  tends to increase the risk level on the positive- $x_0$  side and, in some panels, broadens the high-risk region toward smaller  $x_0$ . This behavior is consistent with correlation-induced alignment between volatility fluctuations and state-noise increments, which enhances the effective impact of volatility bursts on barrier crossing. Conversely, more negative  $\rho$  yields comparatively lower risk and a sharper localization of high risk near the separatrix. Overall, Fig. 5 supports the interpretation that the entropic-risk surface provides a compact diagnostic of basin-sensitive vulnerability under intermittent excitation. The heat maps reveal that correlation not only shifts risk magnitude but also deforms the geometry of risk gradients in the  $(x_0, v_0)$  plane, which is relevant for robust initialization and design under uncertain excitation environments.

Fig. 6 provides a 3D representation of the same risk landscape shown in Fig. 5, offering a complementary view of how the initial entropic risk  $Y_0$  varies with the initial condition  $(x_0, v_0)$  for different correlation levels  $\rho$ . Across panels, the dominant geometric feature is a pronounced rise of  $Y_0$  as  $x_0$  approaches the barrier region and moves into the positive side, which reflects the basin structure of the bistable drift and the associated increase in terminal-loss likelihood. Variations in  $v_0$  modulate the surface height more moderately, with higher initial volatility generally lifting the risk level, particularly near the separatrix where diffusion amplification most effectively promotes barrier approach. Changing  $\rho$  deforms the surface by shifting and tilting the high-gradient region in  $x_0$ , consistent with correlation altering how volatility fluctuations align with state perturbations. Overall, Fig. 6 confirms and visualizes the risk-gradient structure inferred from the heat maps, while making the relative contributions of  $x_0$ ,  $v_0$ , and  $\rho$  to the risk magnitude more apparent.

Fig. 7 assesses the numerical robustness of the regression Monte Carlo solver through sensitivity of the estimated initial entropic risk  $Y_0$  to discretization and approximation choices. The left panel varies the number of time steps  $N$ , the middle panel varies the Monte Carlo sample size  $M$ , and the right panel varies the polynomial basis degree used in the conditional expectation regression. The time-discretization study indicates that  $Y_0$  changes with  $N$ , reflecting the combined influence of forward SDE discretization error and backward regression error that accumulates across time levels. The non-monotone pattern is typical for coupled forward–backward Monte Carlo schemes when both time discretization and statistical regression interact, and it suggests that a moderate step size may provide a practical balance between bias and variance for the present parameter regime. The sample-size sensitivity shows noticeable variability in  $Y_0$  across the tested  $M$ . This is consistent with the fact that  $U_t = \exp(\gamma\xi)$  can be strongly heterogeneous under intermittent forcing, so that finite-sample regression can under- or over-estimate conditional expectations, especially near maturity. The observed dependence supports reporting uncertainty quantification, for example via repeated runs with different random seeds or bootstrap confidence intervals, when presenting final numerical values. The basis-sensitivity panel shows that the choice of regression basis degree has a material effect on  $Y_0$ . Lower-degree bases may underfit the conditional structure near the barrier region, whereas higher-degree polynomials can introduce instability and overfitting in finite samples. The variation across degrees highlights that the

regression step is a principal source of approximation error, and motivates using mild regularization, cross-validation, or localized basis enrichment near the separatrix to improve stability. Overall, Fig. 7 indicates that while the method is operational, careful calibration of  $N$ ,  $M$ , and basis complexity is necessary for reproducible risk estimates under intermittent stochastic volatility.

## 6. Conclusion

A quadratic BSDE framework has been developed for risk-adjusted quantification of noise-induced switching and overload in bistable nonlinear dynamics driven by stochastic volatility. The forward model incorporates a nonnegative mean-reverting variance process and correlated noise channels, enabling controlled investigation of intermittency and state-intensity coupling. The backward component uses dynamic entropic risk, resulting in a quadratic-growth BSDE. An exponential transform converts the quadratic structure into a martingale representation, which can be estimated by regression Monte Carlo without spatial gridding.

The numerical studies are designed to isolate how volatility clustering and correlation alter tail exposure beyond mean-level switching statistics. Increased volatility tends to enlarge the disparity between probability-based measures and risk-adjusted measures, particularly under stronger risk aversion. Correlation reshapes risk landscapes in the joint state-volatility space and can shift the regions where barrier crossing becomes risk-dominant. The full conditional risk process provides additional time-resolved information that can be interpreted as an early-warning signal when the system approaches the separatrix under elevated volatility.

Extensions include underdamped second-order bistable oscillators, intensity models with jumps or rough components to represent stronger intermittency, and the use of the estimated BSDE control to design variance reduction or risk-sensitive control strategies. These directions preserve the central theme that quadratic BSDEs provide a mathematically rigorous and computationally practical tool for nonlinear stochastic dynamics when tail-aware reliability metrics are required.

## CRedit authorship contribution statement

**Dong Feng:** Writing – review & editing, Writing – original draft, Visualization, Validation, Software, Resources, Methodology, Investigation, Formal analysis, Data curation, Conceptualization.

## Declaration of competing interest

The authors declare that they have no known competing financial interests or personal relationships that could have appeared to influence the work reported in this paper.

## Acknowledgments

This research is supported by the China Scholarship Council (CSC., No. 202308080042). The author also wishes to thank two anonymous reviewers and the editor for their valuable comments on earlier versions of this paper.

## Data availability

Data will be made available on request.

## References

- [1] Li G, Liu T, Wu S, Li D, Ding W, Feng Z. Analysis and control of coexisting attractor transitions in a class of rigid vibro-impact systems. *Int J Non-Linear Mech* 2025;174:105066. <https://doi.org/10.1016/j.ijnonlinmec.2025.105066>.
- [2] Jungelges J, Pavletsov M, Perevalova T. Noise-induced behavioral change driven by transient chaos. *Chaos, Solitons Fractals* 2022;158:112069. <https://doi.org/10.1016/j.chaos.2022.112069>.
- [3] Bashkirtseva IA, Pisarchik AN, Ryashko LB. Coexisting attractors and multistate noise-induced intermittency in a cycle ring of Rulkov neurons. *Mathematics* 2023;11(3):597. <https://doi.org/10.3390/math11030597>.
- [4] Stiller O, Becker A, Kramer L. Noise-induced transitions between attractors in time periodically driven systems. *Phys Rev Lett* 1992;68(25):3670–3. <https://doi.org/10.1103/PhysRevLett.68.3670>.
- [5] Semenov VV. The impact of nonlocal coupling on deterministic and stochastic wavefront propagation in an ensemble of bistable oscillators. *Phys Lett A* 2025; 532:130189. <https://doi.org/10.1016/j.physleta.2024.130189>.
- [6] Worsfold JR, Morris RG. Stochastically bistable growth and decay in the Togashi-Kaneko model. *Phys Rev E* 2025;112(1–1):14131. <https://doi.org/10.1103/PhysRevE.112.14131>.
- [7] Song K, Bonnin M, Traversa FL, Bonani F. Moment-based stochastic analysis of a bistable energy harvester with matching network. *Appl Sci* 2023;13(6):3880. <https://doi.org/10.3390/app13063880>.
- [8] Feng D. A compactor-soil coupling model considering mechanical inertia and its delayed feedback active suspension control. *Int J Non-Linear Mech* 2025;179: 105245. <https://doi.org/10.1016/j.ijnonlinmec.2025.105245>.
- [9] Liu P, Tang J, Guo Y, Li Y. Snap-through behaviors of bistable composite panel in centrifugal environments. *Int J Mech Sci* 2025;288:110036. <https://doi.org/10.1016/j.ijmecsci.2025.110036>.
- [10] Ren L, Zhang W, Dong T, Zhang Y. Snap-through behaviors and nonlinear vibrations of a bistable composite laminated cantilever shell: an experimental and numerical study. *Appl Math Mech-Engl Ed* 2024;45(5):779–94. <https://doi.org/10.1007/s10483-024-3111-7>.
- [11] Nadkarni N, Daraio C, Kochmann DM. Dynamics of periodic mechanical structures containing bistable elastic elements: from elastic to solitary wave propagation. *Phys Rev E Stat Nonlinear Soft Matter Phys* 2014;90(2):23204. <https://doi.org/10.1103/PhysRevE.90.023204>.
- [12] Chekroun MD, Koren I, Liu H, Liu H. Generic generation of noise-driven chaos in stochastic time delay systems: bridging the gap with high-end simulations. *Sci Adv* 2022;8. <https://doi.org/10.1126/sciadv.abq7137>.

- [13] Vellela M, Qian H. Stochastic dynamics and non-equilibrium thermodynamics of a bistable chemical system: the Schlögl model revisited. *J R Soc Interface* 2009; 6(39):925–40. <https://doi.org/10.1098/rsif.2008.0476>.
- [14] Artyomov MN, Das J, Kardar M, Chakraborty AK. Purely stochastic binary decisions in cell signaling models without underlying deterministic bistabilities. *Proc Natl Acad Sci USA* 2007;104(48):18958–63. <https://doi.org/10.1073/pnas.0706110104>.
- [15] Spagnolo B, Valenti D. Volatility effects on the escape time in financial market models. *Int J Bifurcation Chaos* 2008;18(09):2775–86. <https://doi.org/10.1142/S0218127408022007>.
- [16] Valenti D, Fazio G, Spagnolo B. Stabilizing effect of volatility in financial markets. *Phys Rev E* 2018;97(6–1):62307. <https://doi.org/10.1103/PhysRevE.97.062307>.
- [17] Bonanno G, Valenti D, Spagnolo B. Role of noise in a market model with stochastic volatility. *Eur Phys J B* 2006;53(3):405–9. <https://doi.org/10.1140/epjb/e2006-00388-1>.
- [18] Bonanno G, Valenti D, Spagnolo B. Mean escape time in a system with stochastic volatility. *Phys Rev E Stat Nonlinear Soft Matter Phys* 2007;75(1 Pt 2):16106. <https://doi.org/10.1103/PhysRevE.75.016106>.
- [19] Valenti D, Spagnolo B, Bonanno G. Hitting time distributions in financial markets. *Physica A Stat Mech Appl* 2007;382(1):311–20. <https://doi.org/10.1016/j.physa.2007.03.044>.
- [20] Fang X, Lou J, Wang J, Chuang K-C, Wu HM, Huang ZL. A self-excited bistable oscillator with a light-powered liquid crystal elastomer. *Int J Mech Sci* 2024;271:109124. <https://doi.org/10.1016/j.ijmecsci.2024.109124>.
- [21] Demenev AA, Yaremkevich DD, Scherbakov AV, Kukhtaruk SM, Gavrilov SS, Yakovlev DR, et al. Ultrafast strain-induced switching of a bistable cavity-polariton system. *Phys Rev B* 2019;100(10):100301. <https://doi.org/10.1103/PhysRevB.100.100301>.
- [22] Klaas M, Sigurdsson H, Liew TCH, Klembt S, Amthor M, Hartmann F, et al. Electrical and optical switching in the bistable regime of an electrically injected polariton laser. *Phys Rev B* 2017;96(4):41301. <https://doi.org/10.1103/PhysRevB.96.041301>.
- [23] Graham R, Ti T. On the weak-noise limit of Fokker-Planck models. *J Stat Phys* 1984;35(5–6):729–48. <https://doi.org/10.1007/BF01010830>.
- [24] Graham R, Tél T. Weak-noise limit of Fokker-Planck models and nondifferentiable potentials for dissipative dynamical systems. *Phys Rev A Gen Phys* 1985;31(2):1109–22. <https://doi.org/10.1103/PhysRevA.31.1109>.
- [25] Feng D, Fu C, Liu P. A modified Johnson-Kendall-Roberts contact model for pavement engineering: consideration of time-dependent surface energy. *Powder Technol* 2026;468:121701. <https://doi.org/10.1016/j.powtec.2025.121701>.
- [26] Alexandrov DV, Bashkirtseva IA, Ryashko LB. Variability in the noise-induced modes of climate dynamics. *Phys Lett A* 2020;384(19):126411. <https://doi.org/10.1016/j.physleta.2020.126411>.
- [27] Mohamad MA, Sapsis TP. Probabilistic description of extreme events in intermittently unstable dynamical systems excited by correlated stochastic processes. *SIAM-ASA J Uncertain Quantif* 2015;3(1):709–36. <https://doi.org/10.1137/140978235>.
- [28] Del Sarto G, Flandoli F. A non-autonomous framework for climate change and extreme weather events increase in a stochastic energy balance model. *Chaos* 2024;34(9). <https://doi.org/10.1063/5.0223309>.
- [29] Gong X-L, Liu X-H, Xiong X, Zhuang X-T. Modeling volatility dynamics using non-Gaussian stochastic volatility model based on band matrix routine. *Chaos, Solitons Fractals* 2018;114:193–201. <https://doi.org/10.1016/j.chaos.2018.07.010>.
- [30] Simonato J-G, Denault M. Multiperiod portfolio allocation: a study of volatility clustering, non-normalities and predictable returns. *N Am J Econ Financ* 2023; 68:101997. <https://doi.org/10.1016/j.najef.2023.101997>.
- [31] Li T, Desmond AF, Stengos T. Dimension reduction via penalized GLMs for non-Gaussian response: application to stock market volatility. *JRFM* 2021;14(12): 583. <https://doi.org/10.3390/jrfm14120583>.
- [32] Bergmann DR, Oliveira MA. Extreme risk clustering in long-memory financial series. *Chaos, Solitons Fractals* 2026;202:117513. <https://doi.org/10.1016/j.chaos.2025.117513>.
- [33] Krawiecki A, Holyst JA, Helbing D. Volatility clustering and scaling for financial time series due to attractor bubbling. *Phys Rev Lett* 2002;89(15):158701. <https://doi.org/10.1103/PhysRevLett.89.158701>.
- [34] Trapin L. Can volatility models explain extreme events?\*. *J Financ Econ* 2018;16(2):297–315. <https://doi.org/10.1093/jffinec/nbx031>.
- [35] Föllmer H, Knispel T. Entropic risk measures: coherence vs. convexity, model ambiguity and robust large deviations. *Stoch Dyn* 2011;11(02n03):333–51. <https://doi.org/10.1142/S0219493711003334>.
- [36] Baier C, Chatterjee K, Megendorfer T, Piribauer J. Entropic risk for turn-based stochastic games. *Inf Comput* 2024;301:105214. <https://doi.org/10.1016/j.ic.2024.105214>.
- [37] Chong WF, Hu Y, Liang G, Zariphopoulou T. An ergodic BSDE approach to forward entropic risk measures: representation and large-maturity behavior. *Finance Stochast* 2019;23(1):239–73. <https://doi.org/10.1007/s00780-018-0377-3>.
- [38] El Karoui N, Peng S, Quenez MC. Backward stochastic differential equations in finance. *Math Financ* 1997;7(1):1–71. <https://doi.org/10.1111/1467-9965.00022>.
- [39] Pardoux E, Peng SG. Adapted solution of a backward stochastic differential equation. *Syst Control Lett* 1990;14(1):55–61. [https://doi.org/10.1016/0167-6911\(90\)90082-6](https://doi.org/10.1016/0167-6911(90)90082-6).
- [40] Richou A. Markovian quadratic and superquadratic BSDEs with an unbounded terminal condition. *Stoch Process Appl* 2012;122(9):3173–208. <https://doi.org/10.1016/j.spa.2012.05.015>.
- [41] Cox JC, Ingersoll JE, Ross SA. A theory of the term structure of interest rates. *Econometrica* 1985;53(2):385. <https://doi.org/10.2307/1911242>.
- [42] Llamazares-Elias S, Tocino A. Mean-reverting schemes for solving the CIR model. *J Comput Appl Math* 2023;434:115354. <https://doi.org/10.1016/j.cam.2023.115354>.
- [43] Güler M. Efficient variants of the minimal diffusion formulation of Markov chain ensembles. *Phys Rev E* 2016;93(2):22123. <https://doi.org/10.1103/PhysRevE.93.022123>.
- [44] Itô K. On a formula concerning stochastic differentials. *Nagoya Math J* 1951;3:55–65. <https://doi.org/10.1017/S0027763000012216>.
- [45] Gobet E, Lemor J-P, Warin X. A regression-based Monte Carlo method to solve backward stochastic differential equations. *aop* 2005;15(3):2172–202. <https://doi.org/10.1214/105051605000000412>.
- [46] Fuhrman M. Nonlinear Kolmogorov equations in infinite dimensional spaces: the backward stochastic differential equations approach and applications to optimal control. *aop* 2002;30(3):1397–465. <https://doi.org/10.1214/aop/1029867132>.